Conformal Additive Manufacturing for Organ Interface

Manjot Singh

Thesis submitted to the faculty of the Virginia Polytechnic Institute and State University
in partial fulfillment of the requirements for the degree of

Master of Science
In
Industrial and Systems Engineering

Blake Johnson
John L. Robertson
Zhenyu “James” Kong

May 8th 2017
Blacksburg, Virginia

Keywords: biomanufacturing, microfluidics, 3D printing, organ health assessment

Conformal Additive Manufacturing for Organ Interface

Manjot Singh

Abstract

The inability to monitor the molecular trajectories of whole organs throughout the clinically relevant ischemic interval is a critical problem underlying the organ shortage crisis. Here, we report a novel technique for manufacturing conformal microfluidic devices for organ interface. 3D conformal printing was leveraged to engineer and fabricate novel organ-conforming microfluidic devices that endow the interface between microfluidic channels and the organ cortex. Large animal studies reveal microfluidic biopsy samples contain rich diagnostic information, including clinically relevant biomarkers of ischemic pathophysiology. Overall, these results suggest microfluidic biopsy via 3D printed organ-conforming microfluidic devices could shift the paradigm for whole organ preservation and assessment, thereby helping to relieve the organ shortage crisis through increased availability and quality of donor organs.

Conformal Additive Manufacturing for Organ Interface

Manjot Singh

General Audience Abstract

Organ failure is one of the most common cause of morbidity and mortality in humans. Unfortunately, there are not enough donor organs to meet the present demand, often referred to as the organ shortage crisis. To compound the problem, there is lack of understanding of the biological processes occurring in organs during the transplantation interval. Here, we present a method to manufacture a biomedical device using a 3D printing technique to monitor, collect, and isolate diagnostically relevant biological species released during the transplantation interval. This information has the potential to lead to a better understanding of organ health, which ultimately could increase the availability and quality of donor organs.

Acknowledgement

I am sincerely grateful for my committee chair Dr. Blake Johnson for welcoming me into his lab and introducing me to this amazing research area of bio-manufacturing and supporting me through the entire process. As my advisor Dr. Johnson allowed me the opportunities to develop my strengths, grow as a researcher. I am also blessed for having a wonderful masters committee and would like to thank Dr. John L. Robertson and Dr. Zhenyu "James" Kong, for the encouragement, guidance and support throughout this entire process.

I would also like to thank the faculty and staff at Department of Industrial and Systems Engineering for such an engaging curriculum and lectures and all the extra-curricular activities organized through various departmental organizations.

My sincere thanks goes to my labmates: Yuxin Tong, Alexander Haring and Ellen Cesewski for all the stimulating discussions and a healthy collaborative research work.

Finally, I must express my very profound gratitude to my family for providing me with unfailing support and continuous encouragement throughout my years of study.

This thesis truly depicts the true example of interdisciplinary team research work.

Contents

List of Figures

Conformal Additive Manufacturing for Organ Interface

Chapter 1

Introduction

Demand for Objective Organ Assessment Techniques

Organ failure is the most common cause of morbidity and mortality[1-3]. As of March 21, 2017 in US alone, 118,099 people were waiting for organs out of which 98,006 (approximately 83%) were waiting for kidneys and the number of patients with waiting time of more than 5 years or more were 15,840 which accounted for 16.2% of the total patients on the waiting list[4]. Although transplantation saves the lives of patients with organ failure, there is a critical shortage of donor organs[1]. Among the various challenges that underlie the organ shortage crisis[5, 6], the inability to monitor the molecular trajectories of whole organs throughout the clinically-relevant ischemic interval obstructs our ability to objectively assess organ quality[7], thereby limiting donor organ availability and transplant efficacy. For example, a high number of potentially-useful organs (*e.g.*, from extended criteria donors) are discarded due to subjectively-perceived inferior function[8, 9] and preserved under non-optimal conditions due to limited understanding of the ischemic mechanisms that govern transplantation outcome[7]. Importantly, it was recently reported that unique molecular trajectories become active after organism death[10], suggesting that the dynamic molecular trajectories of whole organs throughout the ischemic interval may hold promising diagnostic and assessment value. Unfortunately, the characteristics of such trajectories, and value thereof, are presently unknown due to a lack of integrative biotechnology capable of continuously isolating molecular species from ischemic organs in a transplantation setting. Thus, a technique for monitoring the molecular profiles and trajectories of whole organs throughout the clinically-

relevant ischemic interval could shift the paradigm for relieving the organ shortage crisis. However, such techniques hinge on the coherent integration of biomedical devices and whole organs.

Chapter 2

Literature Review

3D Printing as an Emerging Process for Conformal Manufacturing

3D printing is emerging as a paradigm shifting process for conformal manufacturing, defined as the deposition or forming of material on objects possessing 3D surface topography. Importantly, the ability to continuously deposit material along 3D surface topographies and curvilinear coordinate surfaces derived from medical imaging, geometric characterization, or analytical geometry endows 3D printing with novel conformal manufacturing capabilities. As a result, conformal 3D printing has emerged as a valuable process for creating novel electronic[11-14] and biomedical devices[15, 16]. For instance, a micro extrusion printing was used for the fabrication of a custom nerve scaffolds for nerve repair and regeneration of complex peripheral nerve injuries[15]. In another research, antennas were conformally 3D printed of metallic inks onto convex and concave hemispherical surfaces in the form of conductive meander lines to miniaturize the antennas and develop a fabrication technique in which antennas can be rapidly adapted to new specifications, including other operating frequencies, device sizes, or encapsulated designs that offer enhanced mechanical robustness. As a result, their bandwidth approached the fundamental limit for their size, offering nearly an order of magnitude improvement over rudimentary monopole antenna designs[11]. Sun et al. fabricated a 3D interdigitated micro-battery architectures (3D-IMA) by printing concentrated lithium oxide-based inks. The micro-batteries were composed of

interdigitated, high-aspect ratio cathode and anode structures. These batteries exhibited high areal energy and power densities and could potentially be used to power microdevices[17]. In another research, a new method, embedded-3D printing (e-3DP), was devised for the fabrication of strain sensors within highly conformal and extensible elastomeric matrices. e-3DP allowed soft sensors to be created in nearly arbitrary planar and 3D motifs in a highly programmable and seamless manner[18]. In another research, a bionic ear was generated via 3D printing of a cell-seeded hydrogel matrix in the precise anatomic geometry of a human ear, along with an intertwined conducting polymer consisting of infused silver nanoparticles. This allowed for in vitro culturing of cartilage tissue around an inductive coil antenna in the ear, which enabled readout of inductively-coupled signals from cochlea-shaped electrodes. The printed ear exhibited enhanced auditory sensing for radio frequency reception, and complementary left and right ears can listen to stereo audio music[19]. Thus, 3D printing appears poised to revolutionize the field of whole organ interface. However, next-generation devices for whole organ healthcare not only require the coherent matching of device geometry with organ surface topography, but also require the topographical matching of device functional features with organ anatomy.

3D Printed Microfluidic Devices

To date, 3D printing has been used to pioneer the creation of novel functional materials and devices containing diverse interwoven functional features[11, 15, 18, 20-23]. Among these, 3D printing is revolutionizing the manufacturing of microfluidic devices[23], such as those with novel 3D network designs[24, 25]. Lee et al. used stereolithography to 3D print a helical microchannel to detect pathogenic bacteria using magnetic nanoparticle clusters[25]. In yet another research, stereolithographic 3D printer was used to fabricate 3D printed microfluidic devices with integrated membrane-based valves[24]. Ultimately, given microfluidic devices form the basis for a variety of

critical biological technologies, this represents a critical breakthrough for the development of next-generation biotechnology. For example, the ability to interface conformal microfluidic devices with 3D biology would redefine the design space for next-generation 3D microfluidic devices, 3D printed biomedical devices, and whole organ interface.

Purpose

Here we plan to apply conformal printing methodologies to construct organ-conforming microfluidic devices for quantitative organ assessment. Specifically, we plan to use a combination of medical imaging and conformal 3D printing approach to fabricate anatomical organ-conforming microfluidic interfaces that enable a new technique for non-invasive isolation of biomarkers from the renal cortex, which we refer to as 'microfluidic biopsy'.

Chapter 3

Research Overview

We used a customized 3D printing system to print Silicone conformal microfluidic devices using custom micro-extrusion 3D system which consists of a three-axis industrial dispensing robot (F5200N; Fisnar), digital pressure regulator (Ultimus V; Nordson), and a custom imaging system (**Figure 1**) which was then cured and released from the organ mimicking substrate and sterilized with ethanol spray.

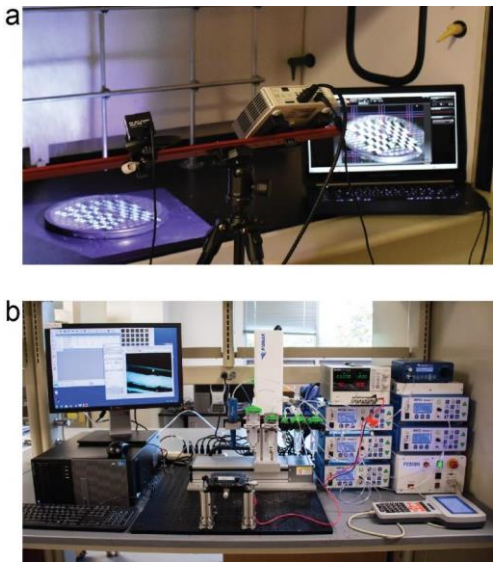

Figure 1 a) Structured-light scanning system for template engineering of kidney geometry. **b)** micro-extrusion 3D printing system used for fabrication of 3D printed conformal microfluidic devices.

The resultant device was then applied to whole organs. The inlet pin of the conformal microfluidic device was first connected to a syringe pump. Prior to interface of the 3D printed conformal microfluidic device with the kidney, an incision was made in the kidney's capsule at the hilus, which coincided with the same location used for template engineering of anatomical device geometry, to create a 3×3 cm^2 flap that was lifted to expose the organ cortex. Subsequently, the device was applied to the organ cortex. Two trans-channel microneedles (27 gauge) were then inserted through the top of the device and 5 mm into the hilus along the channel length. PBS (10 mM; pH 7.4) was then introduced to the device at a flow rate of 100 µL/min. The outlet fluid, referred to as the microfluidic biopsy sample, was continuously collected in 1.5 mL aliquots. The microfluidic biopsy sample acquired at the one hour period was subsequently analyzed using Raman spectroscopy and enzyme-linked immunosorbent assay (ELISA).

The materials used were, phosphate buffered saline (PBS) and Pluronic F127 were from Sigma

Aldrich. Sodium polyacrylate hydrogel was from Hollister. Silicone (SI 595 CL) was from Loctite. Enzyme-linked immunosorbent assay (ELISA) kits for porcine heat shock protein-70 (HSP-70), kidney injury molecule-1 (KIM-1) and β-actin were from Elabscience. Ultrapure de-ionized water (DIW) was obtained from a commercially available DIW system (Direct-Q 3UV; Millipore).

Outcomes:

1) Conformal microfluidic devices were constructed,

2) Molecular species from the whole organs were isolated,

3) Biomarkers of ischemic pathophysiology in these samples were identified.

Concept and Manufacturing Process

The organ cortex contains metabolically active tissue, provides subjective assessment data via traditional biopsy and visual inspection methods, and is influenced by procurement, transportation and preservation processes (*e.g.*, physical handling, ischemic conditions). Thus, the organ cortex is a promising matrix for seeking molecular trajectories that may hold rich diagnostic and assessment value. Of all organs, we hypothesize the renal cortex has significant undiscovered diagnostic value as it is among the most metabolically active regions of the kidney and executes critical physiological processes (*e.g.*, ultrafiltration). Further, the organ shortage crisis is most severe for kidneys due to a lack of effective treatment for end-stage renal disease[26]. Thus, as shown schematically in **Figure 2**, we leveraged a bio-inspired conformal 3D printing approach to fabricate anatomical organ-conforming microfluidic interfaces capable of isolating molecular species from the renal cortex, which we refer to as ‘microfluidic biopsy’.

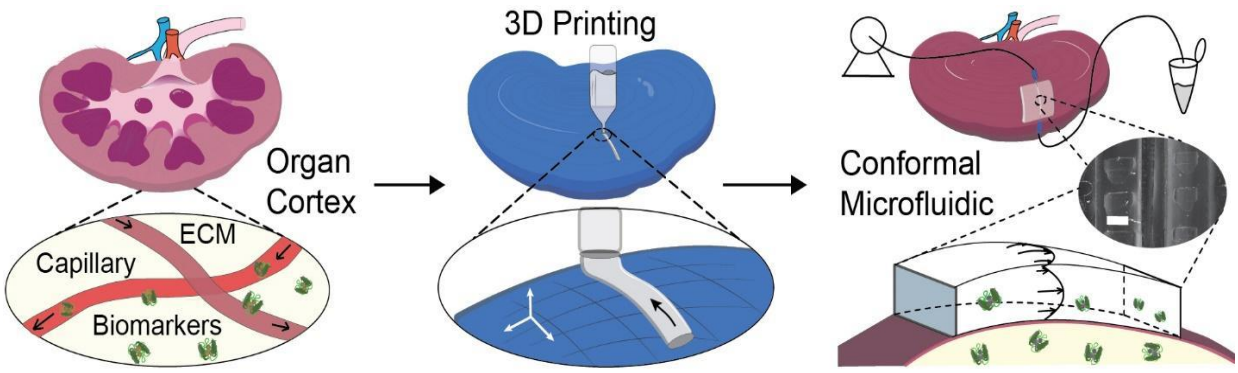

Figure 2 Schematic of the microfluidic biopsy concept for isolating biomarkers from the cortex of whole organs using 3D printed conformal microfluidic devices (scale bar = 500 μm).

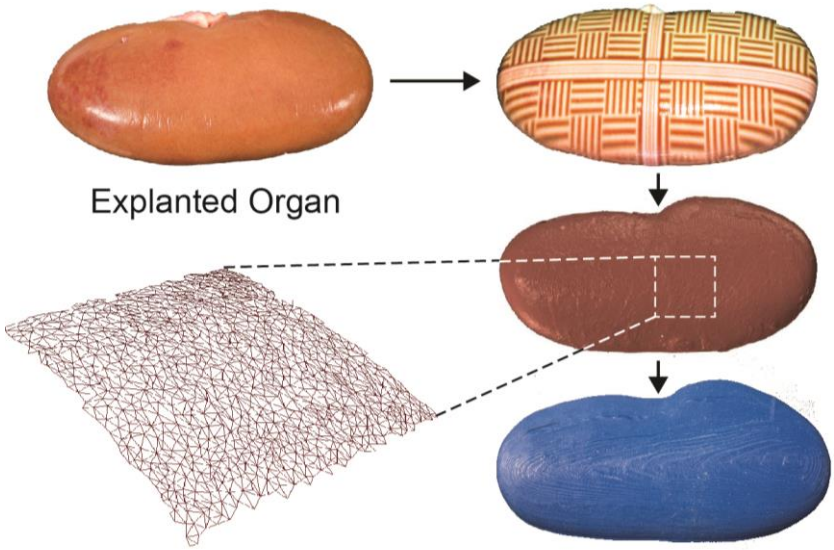

Figure 3 Template engineering process for converting anatomical geometry of whole organs into both 3D printer path information and anatomical substrates for 3D printing (shown in order are explanted kidneys, kidneys exposed to structured-light, digital reconstructions of kidneys, and 3D printed models of kidneys used as biomimetic substrates; expanded region shows the digitized 3D surface topography at the device interface location).

As shown by the last panel of **Figure 2**, the microfluidic biopsy concept is founded on the spontaneous transfer of biomarkers from the organ cortex to an adjacent microfluidic stream established by the 3D printed organ-conforming microfluidic device. Thus, profiling the outlet fluid of the organ-conforming microfluidic device, referred to as the microfluidic biopsy sample, enables real-time monitoring of whole organ molecular trajectories (*e.g.*, molecular clustering and biomarker expression levels). As shown in **Figure 3,** we first digitized whole kidneys using structured-light scanning to both generate 3D surface topography data required for conformal manufacturing and create a biomimetic substrate for conformal 3D printing (see Figure 1). Following the template engineering process, microfluidic devices were printed directly on the biomimetic substrates and subsequently coated with a thin hydrogel layer (see **Figure 4** for additional manufacturing highlights).

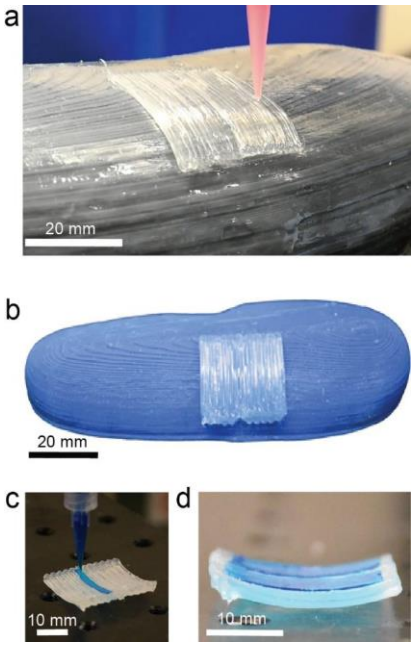

Figure 4 Photograph of the conformal microfluidic device printed on an anatomical substrate derived from medical imaging of porcine kidneys shown during the printing process **(a)** and post-printing **(b)** Photograph of the hydrogel adhesion layer of the conformal microfluidic device shown

during the printing process **(c)** and post-printing **(d)** (blue dye used for visual contrast).

Chapter 4

Methods and Materials

Models of whole kidneys were first printed using a commercially-available plastic 3D printer (Printrbot Simple Metal; Printrbot) based on the digitized kidney data to provide substrates for conformal printing. The organ-conforming microfluidic devices were then printed using a custom microextrusion-based 3D printing system, which has been described previously.[12, 15, 21, 22] The system consisted of a three-axis industrial dispensing robot (F5200N; Fisnar), digital pressure regulator (Ultimus V; Nordson), and a custom imaging system (see **Figure 1**). Path information for the conformal microfluidic devices was constructed based on the 3D surface topograpical data acquired by structured-light scanning. Conformal microfluidic devices were printed using silicone with a 16 - 20 gauge tapered tip, extrusion pressure of *ca.* 10 psi, and printing speed of *ca.* 2 mm/s. The build time was *ca.* one hour. Following printing, the devices were cured, released from the organ substrate, and sterilized with ethanol spray. To provide an adhesion layer for bonding to whole organs, the 3D surface topographical data was subsequently used to apply a thin hydrogel layer (sodium polyacrylate or 30 wt% Pluronic F127) across device's organ contact surface, with the exception of the microchannel. Hydrogel 3D printing was done using a 27 tapered tip (Nordson EFD), extrusion pressure of *ca.* 12 psi, and printing speed of *ca.* 1 mm/s. The build time was *ca.* 30 minutes. Subsequently, hollow pins were inserted into the microchannel inlet and outlet to provide interface with external fluid handling supplies and instrumentation (*i.e.*, tubing, syringe pump and sample collection reservoir).

Having shown the ability to manufacture microfluidic devices on biomimetic substrates, we next verified the 3D topographical matching between the 3D printed microfluidic device and the organ anatomy at the interface location (the hilus of the kidney). As shown in **Figure 5a**, the curvilinear coordinate lines of the device and organ surface were topographically aligned, thereby confirming device-organ coherence.

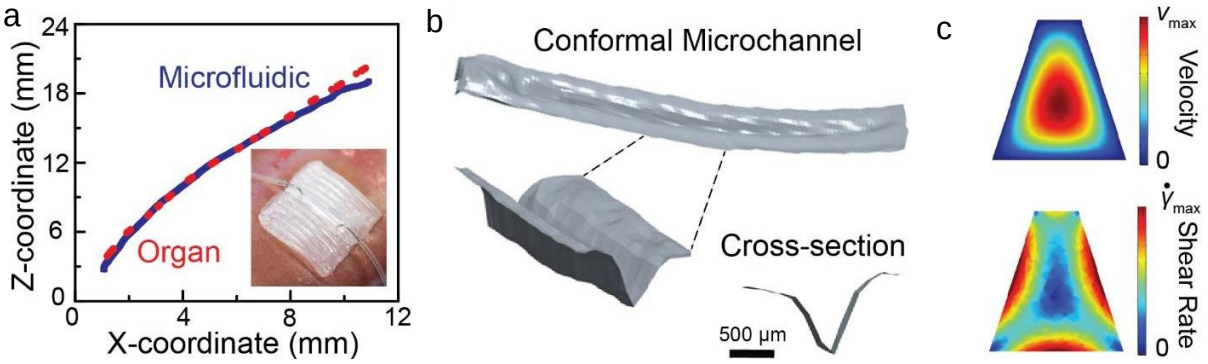

Figure 5 a) Topographical comparison between the organ and the 3D printed conformal microfluidic device at the interface location. **b)** 3D topographical characterization of the 3D printed conformal microchannel. **c)** Fully developed velocity and shear rate profiles present in the 3D printed conformal microfluidic device.

Topographical data for comparison of the 3D printed conformal microfluidic device and organ curvature were obtained using structured-light scanning. 3D printed conformal microfluidic devices were first mounted vertically on a flat substrate. Subsequently, the devices were coated with a thin film of contrast agent (Magnaflux). Prior to imaging, the system was calibrated following vendor-provided protocols using a 30 mm calibration grid. The devices were then scanned and water-tight 3D models were generated as described for structured-light scanning of kidneys. The point cloud data on the kidney and device surfaces corresponding to the organ-device

interface location were first isolated. Subsequently, a 0.2 mm wide band across each data set was isolated. The coordinates from each data set were then processed using the following approach to extract the topographical curvature (i.e. the curvilinear coordinate lines). Using the organ data set as a basis, the coordinates from the device data set were first rotated through a rotation matrix until the unit normal vector at the center of the device coordinate line aligned with the unit normal vector at the center of the organ coordinate line. Subsequently the coordinate lines were shifted into the first quadrant by linearly transforming each set. Non-conformal microfluidic devices printed on flat substrates served as a control for comparing the device-organ 3D topographical matching. The data from control devices was analyzed identically to the conformal microfluidic devices.

Device

Given the microfluidic biopsy concept is founded on the spontaneous transfer of molecular species from the organ cortex into an adjacent microfluidic stream established by the 3D printed organ-conforming microfluidic device, we next characterized the 3D topography and flow characteristics of the conformal microfluidic channel. As shown in **Figure 2**, the 3D printed conformal microfluidic device contains an open basal microchannel. Thus, application of the conformal microfluidic device to the organ establishes a sealed microchannel in which the organ cortex forms the bottom surface. We next used structured-light scanning to characterize the 3D topography of the conformal microchannel. As shown in **Figure 5b**, the conformal microchannel exhibited a trapezoidal cross-section to maximize the organ contact area and showed identical topographical matching to the device-organ contact surfaces. The hydraulic diameter of the conformal channel was 600 μm. Having characterized the 3D topography of the printed conformal microchannel, we next examined the flow characteristics in the device using 3D computational fluid dynamics (CFD)

studies. Our studies revealed the organ cortex is in contact with a microfluidic stream that has a fully developed velocity profile along the vast majority of the microchannel (L ~ 15 mm) (*i.e.*, the microfluidic biopsy location). **Figure 5c** shows the fully developed velocity and shear rate profiles in the conformal microchannel. Such a result is consistent with the theoretical hydrodynamic entry length for internal laminar flow, which predicts the velocity profile becomes fully developed after 143 μm. Collectively, the data shown in **Figure 2-5** demonstrate that 3D printed conformal microfluidic devices form coherent interfaces with whole organs and can establish controlled fluid flow across the organ cortex, thus serving as a potential sink for continuously isolating molecular species.

Having demonstrated the ability to interface 3D printed conformal microfluidic devices with whole organs and establish developed laminar flow across the 3D organ cortex, we next examined if molecular species from the organ cortex spontaneously transfer into the organ-conforming microfluidic stream. Toward this objective, we conducted large animal studies that explored the effect of ischemic conditions on the molecular trajectory of whole organs throughout the clinically relevant ischemic interval using the microfluidic biopsy technique. As shown schematically in **Figure 6a**, our first study investigated the molecular clustering profiles from kidneys exposed to normothermia (NT) and traditional cold storage hypothermia (HT). A photograph of the 3D printed conformal microfluidic device and schematic of the microfluidic biopsy principle is shown in **Figure 6b**.

Chapter 5

Experiments and Analysis

Microfluidic Biopsy Measurements

The inlet pin of the conformal microfluidic device was first connected to a syringe pump. Prior to interfacing the 3D printed conformal microfluidic device with the kidney, an incision was made in the kidney's capsule at the hilus, which coincided with the same location used for template engineering of anatomical device geometry, to create a 3×3 cm^2 flap that could be lifted to expose the organ cortex. Subsequently, the device was applied to the organ cortex. Two trans-channel microneedles (27 gauge) were then inserted through the top of the device and 5 mm into the hilus along the channel length. PBS (10 mM; pH 7.4) was then introduced to the device at a flow rate of 100 µL/min to support the spontaneous transfer of biomarkers into the fluid channel and remained throughout the biopsy interval. The outlet fluid, referred to as the microfluidic biopsy sample, was continuously collected in 1.5 mL aliquots. The microfluidic biopsy sample acquired at the one hour period was subsequently analyzed using Raman spectroscopy and enzyme-linked immunosorbent assay (ELISA).

We first conducted control studies by comparing the molecular clustering profiles of microfluidic biopsy samples acquired from the normothermic group (n = 13 organs) with a control (Neg) group that consisted of input saline solution (n = 13 samples).

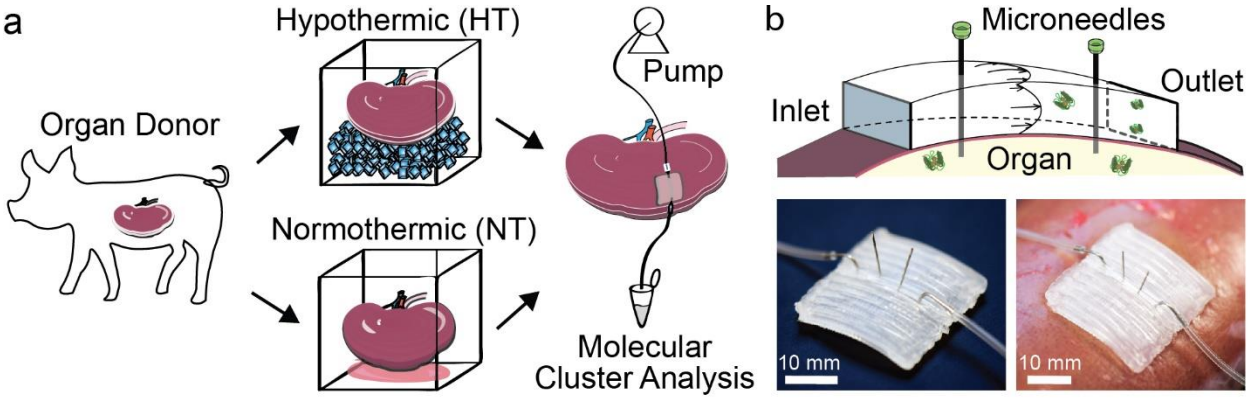

Figure 6 a) Schematic of the large animal study for testing the effect of ischemic conditions on the molecular cluster profile of microfluidic biopsy samples. **b)** Schematic and photographs of the 3D printed conformal microfluidic device used for microfluidic biopsy showing the principle and integration of trans-channel microneedles.

Raman Spectroscopy

Molecular cluster analysis (i.e., bio-fingerprinting) of microfluidic biopsy samples was conducted using Raman spectroscopy (Desktop L-PeakSeeker; Agiltron). The Raman spectrum of each sample was collected using vendor-provided software (PeakSeeker) over 250 -1950 cm-1 with a step size of (1 cm^{-1}) using a 785 nm laser. Ten scans were conducted per sample. Scans were collected with an integration time of 15 s and a delay time of 15 s (see **Figure 6** for representative Raman spectra). After data collection, all dialysate scans were statistically analyzed using principal component analysis (PCA) and discriminant analysis of principal components (DAPC). Briefly, the raw spectral data was first baselined and normalized. Subsequently, all scans within a given experimental group were classified using PCA and DAPC yielding an output representation of each spectrum in terms of canonical values that describe at least 90% of the outcome (e.g., canonical 1 and canonical 2). P-values (p) associated with the statistical

significance of differences between two means (i.e., mean center of mass coordinates for a given experimental group) were calculated using a two-tailed Student t-test assuming unequal variances.

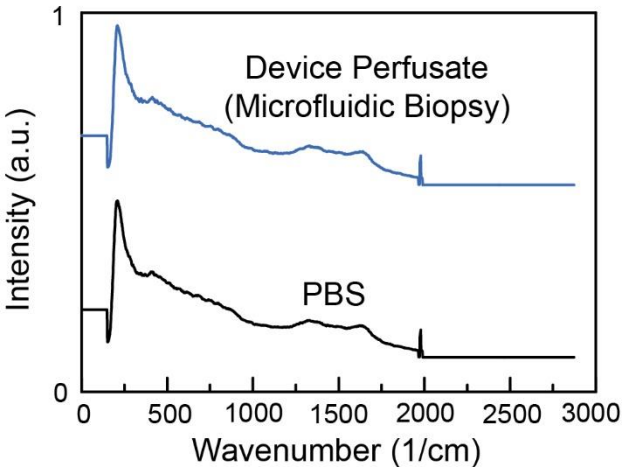

Figure 7 Representative Raman spectra of a microfluidic biopsy sample and negative control (PBS) used as the inputs for principal component analysis (PCA) and discriminant analysis of principal components (DAPC).

As shown in **Figure 8a**, the molecular clustering profiles of the normothermic group and the control group exhibited statistically significant differences in the center of mass (CM) location in the two-dimensional canonical plane ($p < 0.001$). For example, the CM for the normothermic group and the control group was located at (-0.59, 0) and (4.71, 0), respectively ($p < 0.001$; n_{NT} = 1040 and n_{Neg} = 130 points per cluster). Given the only difference between the samples in each group was exposure to the organ cortex, the results suggest that molecular species are spontaneously transferred from the organ cortex to the organ-conforming microfluidic stream. Thus, we next compared the molecular clustering profiles of microfluidic biopsy samples acquired from the normothermic group with the traditional cold storage hypothermic group using a paired organ study. Importantly, **Figure 8b** shows the molecular clustering profiles of the normothermic

group (n = 6 paired organs) and traditional cold storage hypothermic group (n = 6 paired organs) exhibited statistically significant differences in CM. For example, the CM for the normothermic group and the traditional cold storage hypothermic group was located at (1.84, 0) and (-1.84, 0), respectively ($p < 0.001$; $n_{NT} = 480$ and $n_{HT} = 480$ points per cluster). Given the only difference between the samples in each group was the ischemic conditions, as the use of paired organs controlled for animal-to-animal variations, the results suggest that the molecular trajectories of whole organs depend on the ischemic conditions. As shown in **Figure 8c**, distinctive clustering of normothermic and traditional cold storage hypothermic groups was also observed when examining microfluidic biopsy samples acquired from both paired and non-paired organs (n = 25 organs total; n = 32 negative control samples; $n_{NT} = 1520$, $n_{HT} = 480$, $n_{Neg} = 320$ points per cluster).

To examine the sensitivity of the molecular clustering profile (i.e. the population of isolated molecular species) to variations in the ischemic conditions, we next acquired microfluidic biopsy samples from organs that were subjected to machine perfusion throughout the hypothermic ischemic interval (see **Figure 9** for details on the experimental setup).

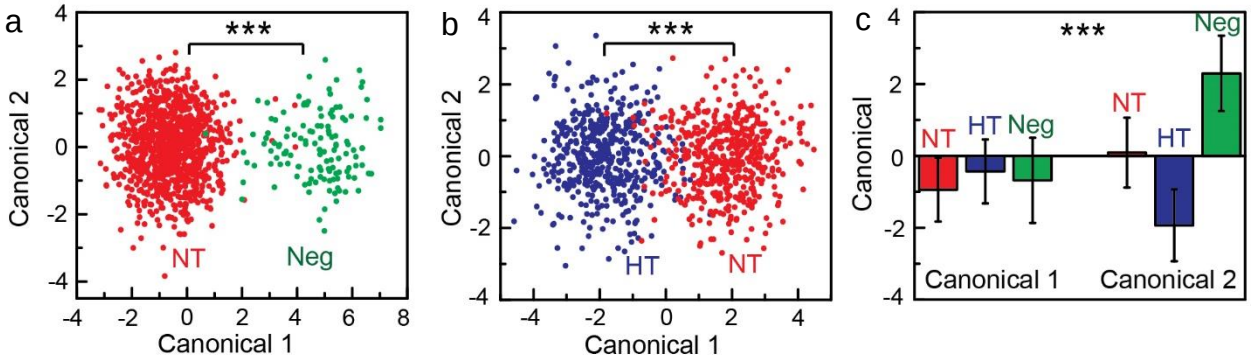

Figure 8 a) Molecular cluster analysis comparing microfluidic biopsy samples acquired from

organs subjected to normothermia (NT) vs. a PBS negative control (Neg). **b)** Molecular cluster analysis comparing microfluidic biopsy samples acquired from paired organs subjected to either normothermia (NT) or traditional cold storage hypothermia (HT).

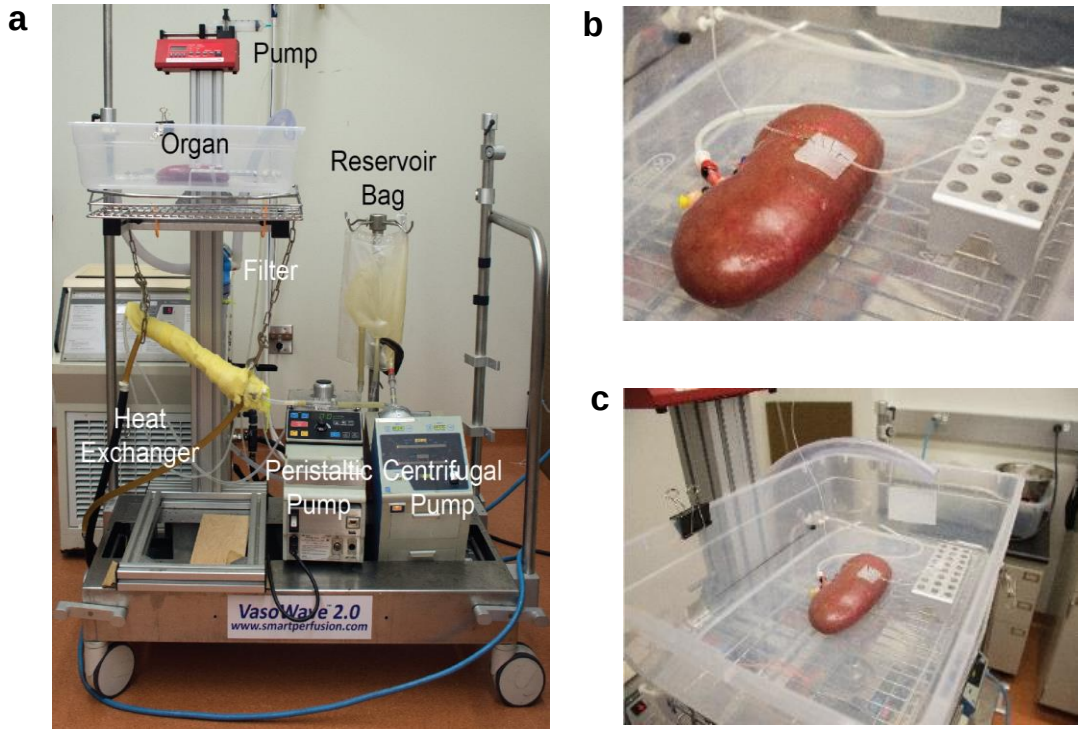

Figure 9 a) Hypothermic machine perfusion organ preservation system with its critical components highlighted. **b)** Photograph of a kidney undergoing microfluidic biopsy on the machine perfusion system described in panel a. **c)** Close up view of panel b.

As shown in **Figure 10**, the molecular clustering profile of the machine-perfused hypothermic group (n = 7 organs) showed a statistically significant difference from the traditional cold storage hypothermic group, the normothermic group and the control group. For example, the CM for the normothermic group, the traditional cold storage hypothermic group, the machine-

perfused hypothermic group and the negative control group was located at (-0.94, 0.89), (-0.43, -1.93), (3.87, 0.12), and (-0.68, 2.30), respectively ($p < 0.001$; n_{NT} =1520, n_{HT} = 480, n_{NT-P} = 480, n_{Neg} = 320 points per cluster).

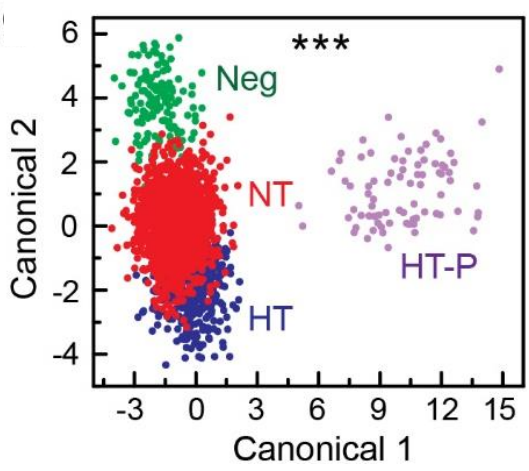

Figure 10 Comparison of molecular cluster profiles among all organs subjected to normothermia (NT), traditional cold storage hypothermia (HT), machine-perfused hypothermia (HT-P) and negative controls (Neg). Triple asterisks indicates $p < 0.001$ among all clusters

The results in **Figs. 6-10** indicate multiple critical findings: 1) the microfluidic biopsy technique provides a novel approach for isolating molecular species from the renal cortex; 2) the populations of isolated molecular species depend on the ischemic conditions; 3) whole organs exhibit dynamic molecular trajectories throughout the ischemic interval; and 4) the microfluidic biopsy technique enables monitoring of whole organ molecular trajectories throughout the clinically relevant ischemic interval.

Enzyme-linked Immunosorbent Assay

The concentrations of HSP-70, KIM-1, and β-actin in the microfluidic biopsy samples were quantified using commercially-available ELISA kits according to vendor-provided protocols.

Briefly, a standard solution was first serially diluted over the ng/mL - pg/mL range. Subsequently, 100 µL of standard, microfluidic biopsy sample, or control was added to each well and incubated for 90 minutes at 37 ^{o}C. The liquid was then removed, each well was washed, and 100 µL of biotinylated detection antibody was added to each well and incubated for one hour at 37 ^{o}C. The liquid from each well was then aspirated and each well was washed with wash buffer. Subsequently, 100 µL of horseradish peroxidase conjugate was added and incubated for 30 minutes at 37 ^{o}C. The liquid from each well was again aspirated and the well was washed with wash buffer. Following the wash step, 90 µL of substrate reagent was added and incubated for 15 minutes at 37 ^{o}C. Next, 50 µL of stop solution was added and the absorbance of the microplates were read at 450 nm. All microplates were analyzed using a multi-mode fluorescence microplate reader (Synergy H1m; BioTek). The average absorbance value for each experimental organ group (i.e., normothermic, traditional cold storage hypothermic, and machine-perfused hypothermic) and the negative control group were calculated. A standard curve was created by plotting the absorbance value at each concentration of the serially diluted standard and fitting a linear best-fit curve to the data. The concentrations of proteins in the experimental samples were then obtained using the average absorbance value and the calibration curve. The concentrations were then scaled based on the internal controls. P-values (p) associated with the statistical significance of differences between two means (i.e., mean concentration of a given experimental group) were calculated using a two-tailed Student t-test assuming unequal variances.

Various biomarkers have been identified in circulating body fluids and organ tissue as diagnostic tools for kidney transplantation via blood and urine analysis and traditional biopsy techniques, respectively[27]. Among these, heat shock protein-70 (HSP-70) and kidney injury

molecule-1 (KIM-1) have been identified as important biomarkers ischemic pathophysiology (*i.e.*, ischemic-reperfusion response and acute kidney injury)[28, 29]. Thus, we next quantified the levels of HSP-70 in the microfluidic biopsy samples acquired among all organ groups (*i.e.*, the normothermic group, the traditional cold storage hypothermic group, and the machine-perfused pothermic group). We found HSP-70 present in microfluidic biopsy samples acquired from each group. However, interestingly, the concentration of HSP-70 varied significantly among the organ groups. For example, the concentration of the ranged from tens to hundreds of pg/mL for the normothermic group, the traditional cold storage hypothermic group, and the machine-perfused hypothermic group, respectively (lowest in the normothermic group and highest in the machine-perfused group).

Chapter 6

Conclusion

These results suggest that microfluidic interfaces with whole organs provide a unique new approach for the quantitative assessment of organs throughout the ischemic interval. They also suggest that organs remain metabolically active throughout the ischemic interval and respond to the parameters of the ischemic interval.

New devices and techniques for continuously isolating biomarkers from whole organs throughout the ischemic interval have the potential to relieve the organ shortage crisis. Here we showed for the first time a new technique for isolating molecular species and biomarkers from whole organs based 3D printed organ-conforming microfluidic devices, which we refer to as ‘microfluidic biopsy’. We found that the molecular clustering profiles of microfluidic biopsy samples differ depending on the ischemic conditions of organ preservation. We also found that

differences among molecular clustering profiles correlate with differential levels of biomarker expression. Importantly, the microfluidic biopsy samples contained known biomarkers of ischemic pathophysiology and metabolic activity. Thus, microfluidic biopsy samples contain rich diagnostic information and offer new opportunities for assessing the quality of whole organs within the clinically relevant ischemic interval. This work represents a major advance in microfluidic devices and organ assessment, as microfluidic biopsy enables the monitoring of whole organ molecular trajectories throughout the ischemic interval. As a result, this work offers new opportunities for objectively assessing, monitoring and controlling organ health, and therefore, appears poised to help relieve the organ shortage crisis.

Future Work

There are several areas in which we can further this research. For instance, device's adhesion to the organ surface can be further improved. We can perform RNA sequencing/ metabolomics on the biopsy samples to reveal the presence and quantity of RNA in the microfluidic biopsy sample. The same research can be extended to other organs. We can work on to make an implantable version of this technology to make it more user friendly and readily available for use during transplantations. Further study is required to understand the impact of puncture parameters i.e. the depth of the micro-punctures, number of punctures and the location of punctures and how that will affect the isolation procedure and the damage, if any, it would cause to the organ. Current biopsy methods can assess only a localized region from where the biopsy sample is taken, we can assess whether through microfluidic biopsy we are able to capture global information of the whole organ. Future plans include placing multiple devices on the pole and hilus of the organ. Raman clustering showed time dependence but because of the small sample size it is difficult to claim whether a pattern exists in the temporal patterns or not. More samples can be collected to investigate the

temporal pattern in Raman clustering

References

1. Jochmans, I. & Watson, C.J.E. Taking the Heat Out of Organ Donation. *New Engl. J. Med.* **373**, 477-478 (2015).

2. Abouna, G.M. Organ Shortage Crisis: Problems and Possible Solutions. *Transplantation Proceedings* **40**, 34-38 (2008).

3. Pomfret, E.A. et al. Solving the Organ Shortage Crisis: The 7th Annual American Society of Transplant Surgeons' State-of-the-Art Winter Symposium. *American Journal of Transplantation* **8**, 745-752 (2008).

4. OPTN (2017).

5. Ruhl, C.E., Sayer, B., Byrd-Holt, D. & Brown, D. in Costs of Digestive Diseases. (ed. J.E. Everhart) (National Institutes of Health, 2008).

6. Mohan, S. et al. Discard of Deceased Donor Kidneys in the United States: The Weekend Effect. *Kidney International* **90**, doi: 10.1016/j.kint.2016.1003.1007 (2016).

7. Niemann, C.U. et al. Therapeutic Hypothermia in Deceased Organ Donors and Kidney-Graft Function. *New Engl. J. Med.* **373**, 405-414 (2015).

8. Kim, Y.H. & Lee, M.R. Expanded Criteria Donors. *J Korean Soc Transplant* **24**, 159-164 (2010).

9. Ojo, A.O. et al. Organ donation and utilization in the USA. *American Journal of Transplantation* **4**, 27-37 (2004).

10. Pozhitkov, A.E. et al. Thanatotranscriptome: genes actively expressed after organismal death. *bioRxiv* (2016).

11. Adams, J.J. et al. Conformal Printing of Electrically Small Antennas on Three-Dimensional Surfaces. *Advanced Materials* **23**, 1335-1340 (2011).

12. Kong, Y.L. et al. 3D printed quantum dot light-emitting diodes. *Nano Lett.* **14**, 7017-7023 (2014).

13. Paulsen, J.A., Renn, M., Christenson, K. & Plourde, R. in 2012 Future of Instrumentation International Workshop (FIIW) Proceedings 1-4 (2012).

14. Blumenthal, T., Fratello, V., Nino, G. & Ritala, K., Vol. 8691 86910P-86910P-86919 (2013).

15. Johnson, B.N. et al. 3D Printed Anatomical Nerve Regeneration Pathways. *Advanced Functional Materials* **25**, 6205-6217 (2015).

16. Xu, L. et al. 3D multifunctional integumentary membranes for spatiotemporal cardiac measurements and stimulation across the entire epicardium. *Nat. Comm.* **5**, 3329 (2014).

17. Sun, K. et al. 3D Printing of Interdigitated Li-Ion Microbattery Architectures. *Advanced Materials* **25**, 4539-4543 (2013).

18. Muth, J.T. et al. Embedded 3D Printing of Strain Sensors within Highly Stretchable Elastomers. *Advanced Materials* **26**, 6307-6312 (2014).

19. Mannoor, M.S. et al. 3D Printed Bionic Ears. *Nano letters* **13**, 2634-2639 (2013).

20. Kong, Y.L. et al. 3D printed quantum dot light-emitting diodes. *Nano Letters* **14**, 7017-7023 (2014).

21. Johnson, B.N. et al. 3D printed nervous system on a chip. *Lab on a Chip* **16**, 1393-1400 (2016).

22. Gupta, M.K. et al. 3D Printed Programmable Release Capsules. *Nano Letters* **15**, 5321-5329 (2015).

23. Au, A.K., Huynh, W., Horowitz, L.F. & Folch, A. 3D-Printed Microfluidics. *Angewandte Chemie International Edition* **55**, 3862-3881 (2016).

24. Rogers, C.I., Qaderi, K., Woolley, A.T. & Nordin, G.P. 3D printed microfluidic devices with integrated valves. *Biomicrofluidics* **9**, 016501 (2015).

25. Lee, W. et al. 3D-Printed Microfluidic Device for the Detection of Pathogenic Bacteria Using Size-based Separation in Helical Channel with Trapezoid Cross-Section. *Scientific Reports* **5**, 7717 (2015).

26. Bastani, B. The worsening transplant organ shortage in USA; desperate times demand innovative solutions. *J. Nephropathol.* **4**, 105-109 (2015).

27. Mas, V.R., Mueller, T.F., Archer, K.J. & Maluf, D.G. Identifying biomarkers as diagnostic tools in kidney transplantation. *Expert Rev. Mol. Diagn.* **11**, 183-196 (2011).

28. Bonventre, J.V. Mechanisms of ischemic acute renal failure. *Kidney International* **43**, 1160-1178 (1993).

29. Vaidya, V.S., Ferguson, M.A. & Bonventre, J.V. Biomarkers of Acute Kidney Injury. *Annual Review of Pharmacological Toxicology* **48**, 463-493 (2008).